Optics Communications 518 (2022) 128339

Contents lists available at ScienceDirect

Optics Communications

journal homepage: www.elsevier.com/locate/optcom

Characterizing the temporal rotation and radial twist of the interference pattern of vortex beams

Longzhi Nie [a,c,1], Lingran Kong [a,c,1], Tianyou Gao [a,*], Nenghao Dong [a,c], Kaijun Jiang [a,b,**]

[a] State Key Laboratory of Magnetic Resonance and Atomic and Molecular Physics, Wuhan Institute of Physics and Mathematics, Innovation Academy for Precision Measurement Science and Technology, Chinese Academy of Sciences, Wuhan 430071, China
[b] Center for Cold Atom Physics, Chinese Academy of Sciences, Wuhan 430071, China
[c] University of Chinese Academy of Sciences, Beijing 100049, China

ARTICLE INFO

Keywords:
Vortex beam
Interference pattern
Topological charge
Conjugate light

ABSTRACT

We experimentally and theoretically characterize the temporal rotation and radial twist of the interference pattern of a vortex beam with its conjugate copy. To quantitatively study the temporal rotation and radial twist, we controllably modify the conjugate beam to obtain a frequency or wavefront curvature difference using a movable Mach–Zehnder interferometer. The effects of the physical parameters (i.e., the topological charge, frequency difference and wavefront curvature difference of the vortex beams) on the temporal rotation as well as radial twist are systematically explored. We further measure two parameters, the rotation velocity Ω and twist coefficient α, respectively, to characterize the degree of the temporal rotation and radial twist of the interference pattern. The theory of the interference model on vortex beams has good agreement with the experimental results. This work is helpful for study on the detailed structure of the interference pattern and manipulation of matter with superimposed vortex beams.

1. Introduction

Vortex laser beams possessing an azimuthal phase structure $\exp(il\phi)$ carry orbital angular momentum (OAM) of $l\hbar$ per photon, where l is an integer number, referred to as the topological charge (TC) [1,2]. Laguerre–Gaussian (LG) beam is a typical vortex optical beam. The magnitude of TC expresses the number of 2π phase cycles around the singularity, and the sign indicates the rotation direction of the wavefront around the central axis. Due to the special property with controllable OAMs, the vortex optical beams have been extensively used in diverse research areas, including optical communication [3,4], optical imaging [5], manipulation of mesoscopic objects [6–8], and production of vortex states in ultracold quantum gases [9–13].

Interferometry is a fundamental method to explore the characteristics of the vortex laser beam and its applications [14–22]. The structure of the interference pattern strongly depends on the relative parameters of vortex beams [23–26]. When there exists a frequency or wavefront curvature difference between two interfering vortex beams, the temporal rotation or radial twist will emerge in the interference pattern [27–29], respectively, which has potential applications. For example, the twisted interference fringes were proposed to enhance the gradient force exerted by the Tornado-like pattern upon micro-particles in optical tweezers [30], measure the curvature radius of a concave mirror or convex lens [31], and perform the high-resolution refractive index sensing [32,33]. The rotating interference pattern has broad applications in manipulation of cold atoms, such as generating artificial gauge electromagnetic field [34], exploring quantum Hall physics [35], rotating single atoms [36], and so on. Previous works have observed the rotation and twist effects of the interference pattern mainly based on the visual inspection [27–29,37,38], not providing quantitative information. The knowledge of the detailed structure of the optical interference pattern is required to understand the interaction between matter and superimposed vortex beams. Quantitatively characterizing the temporal rotation and radial twist of the interference pattern is favorite to extend the applications of vortex beams.

In this paper, we quantitatively characterize the temporal rotation and radial twist of the interference pattern of a vortex beam with its conjugate copy. To study the radial twist, we modify the conjugate beam to obtain a wavefront curvature difference using a movable Mach–Zehnder (MZ) interferometer. To study the temporal rotation, we modify the conjugate beam to obtain a frequency difference using two acousto-optic modulators (AOMs). The effects of the physical parameters (i.e., the TC, frequency difference and wavefront curvature

* Corresponding author.
** Corresponding author at: State Key Laboratory of Magnetic Resonance and Atomic and Molecular Physics, Wuhan Institute of Physics and Mathematics, Innovation Academy for Precision Measurement Science and Technology, Chinese Academy of Sciences, Wuhan 430071, China.
E-mail addresses: 602gty@sina.com (T. Gao), kjjiang@wipm.ac.cn (K. Jiang).
[1] The authors contributed equally to this work.

https://doi.org/10.1016/j.optcom.2022.128339
Received 27 January 2022; Received in revised form 8 April 2022; Accepted 13 April 2022
Available online 20 April 2022

difference of the vortex beams) on the temporal rotation as well as the radial twist are explored. We further measure two parameters, the rotation velocity Ω and twist coefficient α, respectively, to characterize the degree of the temporal rotation and radial twist of the interference pattern. The theory of the interference model on vortex beams has good agreement with the experimental results. Here we study the interference between the vortex beam and its conjugate copy. The method demonstrated is also applicable to other kinds of vortex beams.

2. Theoretical analysis

The vortex beam contains a phase singularity where the intensity vanishes [39,40]. For a LG beam, the scaled electric field is

$$E(r,\phi,z,t) = A(r)\exp[-i\theta(r,z)]\exp(-i\omega t)\exp(-il\phi). \tag{1}$$

$$\theta(r,z) = \frac{k}{2}\frac{r^2}{R(z)} + (2p+|l|+1)\arctan(\frac{z}{z_R}) + kz + \vartheta, \tag{2}$$

$$A(r) = E_0 C_{lp}^{LG} L_p^{|l|}(\frac{2r^2}{w^2(z)})\frac{w_0}{w(z)}(\frac{r\sqrt{2}}{w(z)})^{|l|}\exp(-\frac{r^2}{w^2}), \tag{3}$$

where ω is the laser frequency, r is the radius, ϕ is the azimuthal angle, z is the propagation distance, $w(z) = w_0\sqrt{1+(z/z_R)^2}$ is the beam radius and w_0 is the waist radius, $z_R = \pi w_0^2/\lambda$ is the Rayleigh length with the wavelength λ, $k = 2\pi/\lambda$ is the wave vector, $L_p^{|l|}$ is an associated Laguerre polynomial, $C_{lp}^{LG} = \sqrt{\frac{2p!}{\pi(p+|l|)!}}$ is the normalization coefficient, ϑ represents the additional phase shift induced by the optics in the optical path, p is the radial index, and l is the azimuthal index (referred as the TC) [41]. The radius of the wavefront curvature is

$$R(z) = z(1+\frac{z_R^2}{z^2}). \tag{4}$$

We consider the simple case with $p = 0$. By interfering two co-propagating LG beams, we obtain the intensity distribution [27,42],

$$\begin{aligned} I &= \frac{nc\varepsilon}{2}|E_1+E_2|^2 \\ &= \frac{nc\varepsilon}{2}\left[A_1(r)^2 + A_2(r)^2 + 2A_1(r)A_2(r)\cos(-\Delta l\phi - \Delta\omega t - \Delta\theta)\right], \end{aligned} \tag{5}$$

where $\Delta l = l_1 - l_2$, $\Delta\omega = \omega_1 - \omega_2$ and $\Delta\theta = \theta_1 - \theta_2$. ε is the dielectric constant, n is the refractive index, and c is the speed of light. The azimuthal angle for the maximum intensity of the bright interference fringe is

$$\phi_{max}(t) = -\frac{2m\pi + \Delta\omega t + \Delta\theta}{\Delta l}, \tag{6}$$

where m is an integer.

Here we consider that a vortex beam interferes with its conjugate copy. Then $l_2 = -l_1$ and $\Delta l = 2l_1$. From the first term on the right of Eq. (6), the number of the bright interference fringes in one circle equals $|\Delta l|$, twice the magnitude of the TC. The temporal rotation and radial distribution of the bright interference fringes depend on $\Delta\omega$, $\Delta\theta$ and Δl, which are related to the other two terms of Eq. (6). So we will analyze the structure of the interference pattern from two aspects as follows.

First, when there is a frequency difference $\Delta\omega \neq 0$, ϕ_{max} is time-dependent, and the whole interference pattern will rotate around the central axis. The rotation velocity is

$$\Omega = \frac{\partial\phi_{max}}{\partial t} = -\frac{\Delta\omega}{\Delta l}. \tag{7}$$

Adopting the convention of the right-hand coordinate system, when signs of $\Delta\omega$ and Δl are the same, the interference pattern will rotate clockwise ($\Omega < 0$), and vice versa. So with the knowledge of $\Delta\omega$ and Δl, we can determine the temporal rotation of the interference pattern.

Secondly, $\Delta\theta$ in Eq. (6) can be written as

$$\Delta\theta = \Phi(z_1,z_2) + \frac{k}{2}(\frac{1}{R_1(z)} - \frac{1}{R_2(z)})r^2, \tag{8}$$

where the term Φ varying with z is the so-called Gouy phase, and its influence on interference pattern has been discussed in Ref. [43]. ϕ_{max} is r-dependent. In the case $\Delta\omega = 0$, ϕ_{max} is written as

$$\phi_{max} = \alpha r^2 - \frac{2m\pi + \Phi(z_1,z_2)}{\Delta l}, \tag{9}$$

$$\alpha = -\frac{k}{2}\frac{\Delta\rho}{\Delta l} = -\frac{k}{2}\frac{\Delta(\frac{1}{R})}{\Delta l} = -\frac{k}{2}\frac{\frac{1}{R_1(z)} - \frac{1}{R_2(z)}}{\Delta l}, \tag{10}$$

where $\rho = \frac{1}{R}$ is the wavefront curvature. When there is a wavefront curvature difference $\Delta\rho \neq 0$, the interference fringe will twist along the radial direction. α is defined as the twist coefficient. If the signs of $\Delta\rho$ and Δl are the same, i.e., $\alpha < 0$, the interference fringe twists clockwise, and vice versa. So with the knowledge of $\Delta\rho$ and Δl, we can determine the radial twist of the interference fringe. The magnitude of α characterizes the degree of the radial twist. For the case with $p \neq 0$, the beam has the common phase terms $\exp[-ikr^2/(2R(z))]$ and $\exp[-i\omega t]$, so the presented theory should also be valid.

3. Experimental setup

We have theoretically analyzed the temporal rotation and radial twist of the interference pattern in Section 2. Then we will observe these two behaviors in the experiment. Fig. 1 schematically presents the experimental setup. The diode laser with the wavelength $\lambda = 782.7$ nm is a monochromatic laser with a linewidth of about 1.0 MHz. Two laser beams from the same laser have a long coherent length. The fiber is used to obtain a Gaussian beam. A vortex phase plate (VPP) (RPC Photonics, VPP-m780) is used to convert a Gaussian beam into a LG beam with a TC of l_1. The main setup is a MZ interferometer. The sign of the TC will change once the LG beam is reflected [44]. Then the transmitted beam from polarizing beam splitter 1 (PBS1) is reflected four times (M_4, M_1, M_1', M_5), and the TC is still l_1 after PBS2. We call this beam the test beam. The reflected beam from PBS1 is reflected five times (PBS1, M_2, PBS3, M_3, PBS2), and becomes the conjugate beam after PBS2, i.e., $l_2 = -l_1$. The method that we change the sign of the TC by controlling the times of the reflection is simpler than using a Dove prism [38,45]. Also it is convenient to adjust the wavefront curvature difference between the test and conjugate beams, which will be explained later. We use two AOMs (AOM1 with the driving frequency f_1 and AOM2 with f_2) to control the frequencies of the two beams, respectively. The frequencies of the test and conjugate beams are ν_1 and ν_2. Then $f_1 - f_2 = \nu_1 - \nu_2 = \Delta\nu$. The half-wave plate next to the laser rotates the optical polarization to equalize the intensities of the test and conjugate beams after PBS5. The half-wave plate after PBS1 changes the optical polarization from the vertical to the horizontal direction, making the light transmit through PBS3. The quarter-wave plate before M_4 converts the light between the linear and circular polarizations, forming a double-pass configuration. The half-wave plate after PBS2 rotates the optical polarizations to balance the intensities of the two laser beams after PBS4. The polarizations of the two beams after PBS4 are the same, and the interference pattern is probed with a sCMOS camera (model No: pco.edge 4.2).

According to Eq. (4), $R(z)$ is determined by the propagation distance z. VPP is placed at the focus of the beam ($z = 0$). The waist radius is $w_0 = 4.2\times10^{-4}$ m and the Rayleigh length is $z_R = 0.7$ m. We set $z > z_R$ in the experiment, then there is a one-to-one correspondence between $R(z)$ and z. The mirrors (M_1, M_1' and M_2) are movable. We control the distances (z_1, z_2) of the test beam and its conjugate copy by adjusting the positions of mirrors M_1 (M_1') and M_2, respectively. $\Delta z = z_1 - z_2$. The wavefront curvature difference between the two beams can be written as

$$\Delta\rho = \frac{1}{R_1(z)} - \frac{1}{R_2(z)} = \frac{-\Delta z(z_1z_2 - z_R^2)}{(z_1^2+z_R^2)(z_2^2+z_R^2)}. \tag{11}$$

Under the condition $z_{1,2} > z_R$, the signs of Δz and $\Delta\rho$ are opposite. We control the value of $\Delta\rho$ by adjusting Δz.

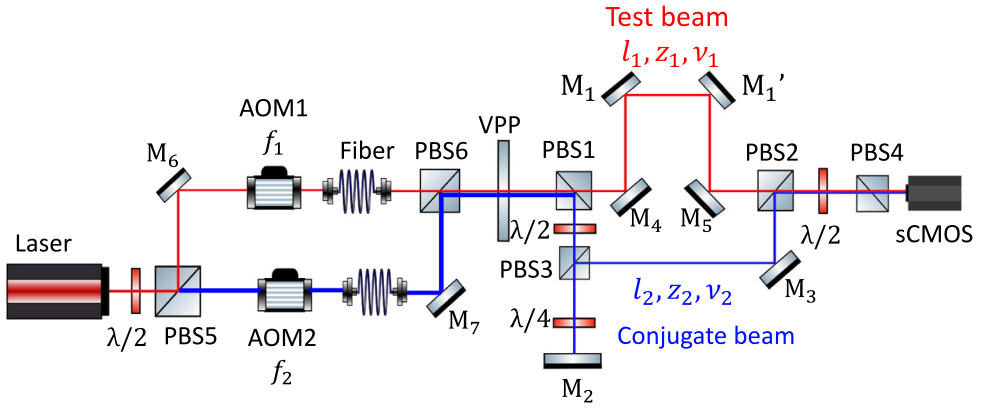

Fig. 1. Experimental setup to measure the interference pattern of the vortex beam with its conjugate copy. The vortex beams are generated after the VPP. The test vortex beam (red lines) and its conjugate copy (blue lines) form a MZ interferometer. l_1 and l_2 are the TCs of the two beams, respectively. The interference pattern is probed with a sCMOS camera. Two AOMs (AOM1 with the driving frequency f_1, AOM2 with f_2) control the frequencies (ν_1, ν_2) of the two beams, respectively. The positions of the mirrors M_1 (M_1') and M_2 control the propagation distances (z_1, z_2) of the two beams, respectively. VPP, vortex phase plate. AOM, acousto-optic modulator. PBS, polarization beam splitter. $\lambda/2$, half-wave plate. $\lambda/4$, quarter-wave plate.

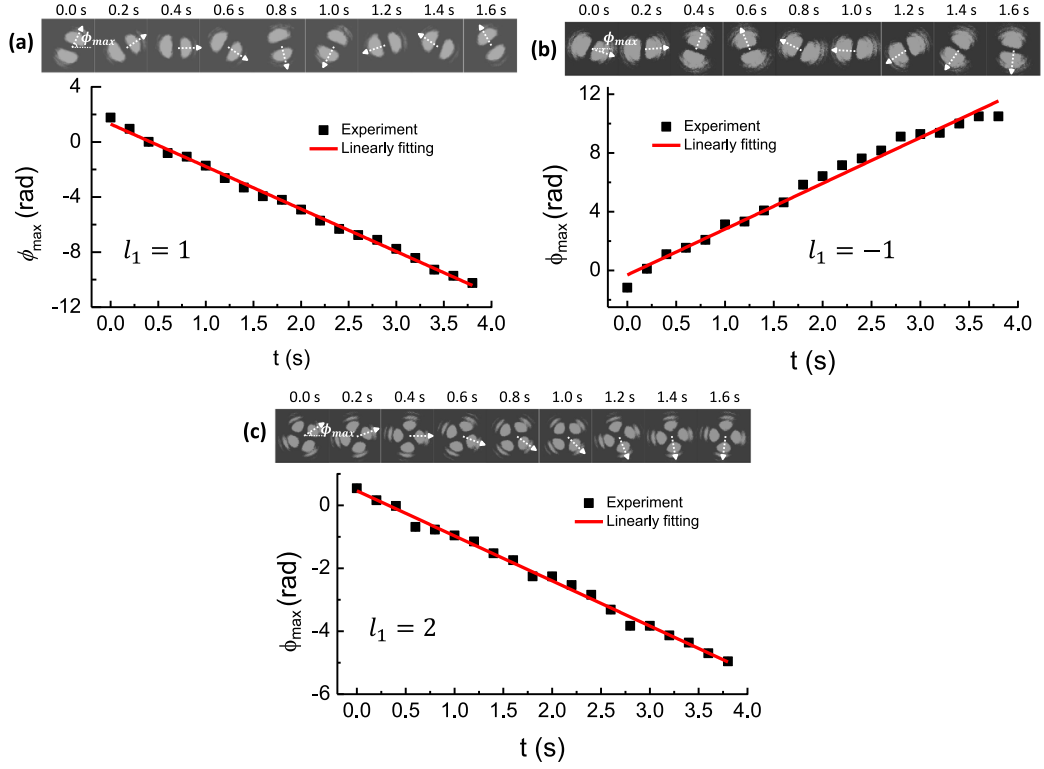

Fig. 2. Temporal rotation of the interference pattern with a frequency difference $\Delta\nu = \nu_1 - \nu_2 = 1$ Hz. (a) is for $l_1 = 1$, (b) for $l_1 = -1$ and (c) for $l_1 = 2$. The upper panel shows the rotating patterns imaged every 0.2 s. ϕ_{max} is the azimuthal angle for the maximum intensity of the bright interference fringe. The lower panel shows ϕ_{max} as a function of the rotation time. The error bars are smaller than the data marks. The red solid line is a linear fitting used to extract the rotation velocity Ω. From the fitting, $\Omega = (-3.11(9),\ 3.04(3),\ -1.61(3))$ rad/s for $l_1 = (1,\ -1,\ 2)$.

4. Results and discussion

4.1. Temporal rotation of the interference pattern

Fig. 2 shows the rotation of the interference pattern with a frequency difference $\Delta\nu = 1$ Hz. Here $z_1 = z_2 = 1.4$ m, and the interference fringe has no radial twist. The number of interference fringes equals $2|l_1|$. The interference pattern rotates clockwise with $l_1 > 0$ (i.e., $l_1 = 1,\ 2$). When the sign of l_1 changes (i.e., $l_1 = -1$), the rotation direction is reversed. Moreover, the rotation for $l_1 = 1$ is faster than that for $l_1 = 2$. All these observations are consistent with predictions of Eq. (7). ϕ_{max} is the azimuthal angle for the maximum intensity of the bright interference fringe. The method to determine ϕ_{max} is shown in Fig. 6. Here the interference fringes have no radial twist and ϕ_{max} is r-independent, so we only need to fit one ring of the interference pattern using a cosine function. The ring is chosen to cover the regions of maximum intensities of the bright interference fringes. The value of ϕ_{max} and its systematic error come from the fitting. To extract the value of rotation velocity Ω, we measure the time evolution of ϕ_{max}, as shown in the lower panel of Fig. 2. We use a linear function $\phi_{max} = \Omega t + \phi_0$ to fit the experimental data, where Ω and ϕ_0 are the fitting parameters. From the fitting, $\Omega = -3.11(9)$ rad/s for $l_1 = 1$, $\Omega = 3.04(3)$ rad/s for $l_1 = -1$, and $\Omega = -1.61(3)$ rad/s for $l_1 = 2$. The value in the parenthesis is the statistic error from the fitting, i.e., $\Omega =$

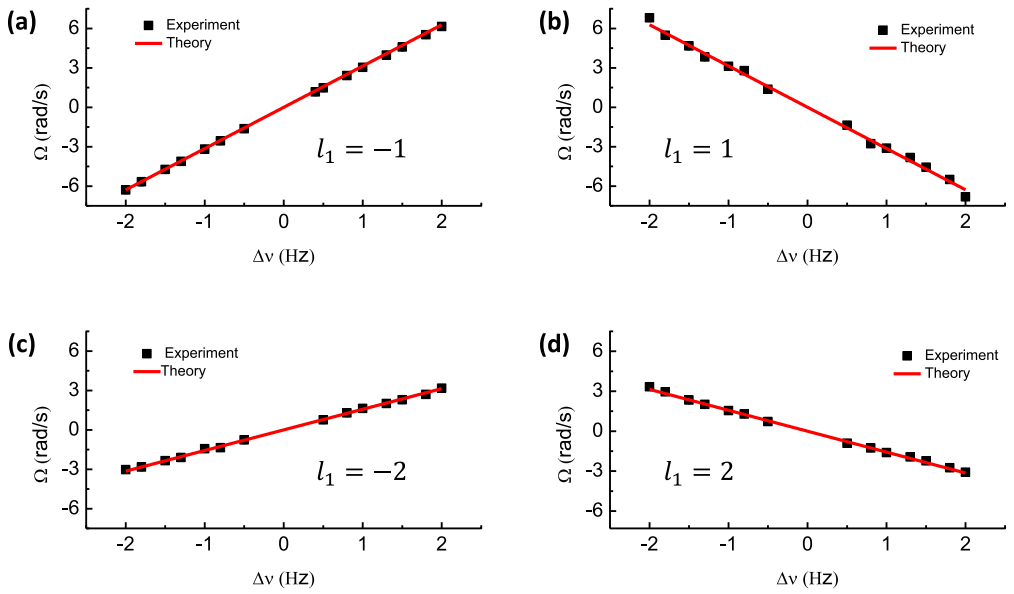

Fig. 3. Rotation velocity Ω for positive and negative TCs. Ω is plotted versus $\Delta\nu$. (a) is for $l_1 = -1$, (b) for $l_1 = 1$, (c) for $l_1 = -2$, and (d) for $l_1 = 2$. The error bars are smaller than the data marks. The red solid line is the theoretical calculation of Eq. (7).

3.04(3) rad/s standing for $\Omega = 3.04 \pm 0.03$ rad/s. From the calculation of Eq. (7), $\Omega = (-3.14,\ 3.14,\ -1.57)$ rad/s for $l_1 = (1,\ -1,\ 2)$. The theoretical calculations have good agreements with the experimental measurements.

In Fig. 3, we measure Ω for positive and negative TCs (i.e., $l_1 = \pm 1,\ \pm 2$). $\Delta\nu$ varies from -2 Hz to 2 Hz. When $\Delta\nu$ is small ($\Delta\nu \approx 0$), the rotation is too slow to be probed. It is shown that when the signs of l_1 and $\Delta\nu$ are the same, $\Omega < 0$, and vice versa. When l_1 is negative (positive), Ω increases (decreases) linearly with increasing $\Delta\nu$. The calculation of Eq. (7) agrees well with the experimental results.

Previous works have observed the images of the rotating interference pattern with a frequency difference [27,28], while the quantitative dependence of the rotation on the physical parameters is yet to be explored. Here we measure the temporal evolution of the parameter ϕ_{max}. We further measure the rotation velocity Ω to quantitatively characterize the temporal rotation of the interference pattern versus the frequency difference $\Delta\nu$ as well as the TC l_1.

4.2. Radial twist of the interference fringe

To study the radial twist of the interference fringe, we set $\Delta\nu = 0$. In this case, the interference pattern is static. Fig. 4 shows the twisted interference patterns with a wavefront curvature difference $\Delta\rho \neq 0$. Under the condition $\Delta z < 0$ (i.e., $\Delta\rho > 0$), if l_1 is positive (i.e., $l_1 = 1,\ 2,\ 3,\ 4$), the interference fringe twists clockwise ($\alpha < 0$). When the sign of l_1 changes (i.e., $l_1 = -1,\ -2,\ -3,\ -4$), the interference fringe twists anti-clockwise ($\alpha > 0$). These twist effects can also be predicted by Eqs. (9) and (10). The calculated interference patterns with Eq. (5) also show obvious radial twists, similar to the experimental results. It is noted that for $l_1 = \pm 1$, Δz is big to clearly show the twist tails.

Fig. 5 schematically shows the effect of the wavefront curvature difference on the radial twist of the interference fringes. $z_1 = 1.4$ m is fixed, and we change z_2 to get different values of Δz. The twist direction of the interference fringes is reversed from the clockwise to anti-clockwise when Δz varies from the positive to negative. The twist effect becomes more obvious when increasing the magnitude of Δz. For $\Delta z = 0$, the twist effect vanishes. These observations are consistent to the predictions of Eqs. (9) and (10).

To quantitatively characterize the twist degree of the interference fringe, we measure the twist coefficient α which quantifies the variation of ϕ_{max} along the radial direction. We take the interference pattern

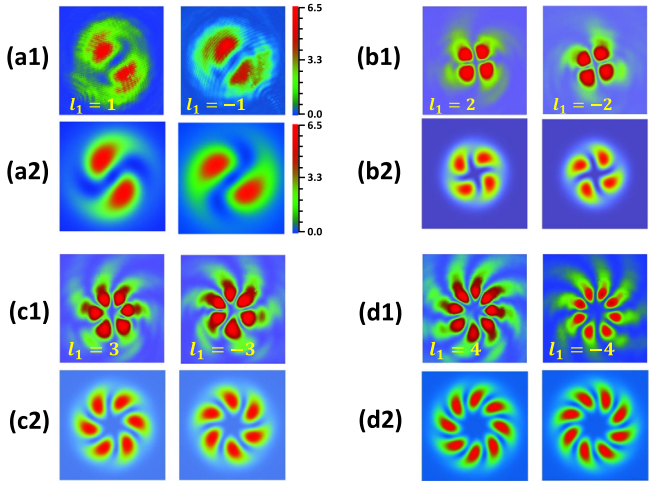

Fig. 4. Twisted interference patterns with a wavefront curvature difference. (a1), (b1), (c1) and (d1) are the experimental observations for $l_1 = \pm 1, \pm 2, \pm 3, \pm 4$, respectively. (a2), (b2), (c2) and (d2) are the corresponding theoretical simulations with Eq. (5). In (a1), $z_1 = 1.1$ m and $z_2 = 2.25$ m. In (b1), (c1) and (d1), $z_1 = 1.4$ m and $z_2 = 2.0$ m.

with $l_1 = -3$ as an example. As shown in Fig. 6(a), we analyze the interference fringe with the radius $r = 1.7$ mm. According to Eq. (5), we use a cosine function $I = I_0 + A \times \cos[-\Delta l(\phi - \phi_{max})]$ to fit the data. Here $\Delta l = 2l_1 = -6$. ϕ_{max} is the azimuthal angle for the maximum intensity of the first bright interference fringe, and its value is set in the range $[-\frac{\pi}{|\Delta l|}, \frac{\pi}{|\Delta l|}]$. It is noted that to optimize the fitting, two circles with $\phi \in (0,\ 4\pi)$ are plotted. From the fitting, $\phi_{max} = 0.086(10)$ rad. Then we plot ϕ_{max} as a function of r in Fig. 6(b). According to Eq. (9), we use a quadratic function $\phi_{max}(r) = \alpha r^2 + \phi_c$ to fit the data, extracting $\alpha = 8.05(17) \times 10^4$ rad m^{-2}. The data in the parenthesis is the statistic error from the fitting. From the calculation of Eq. (10), $\alpha = 8.30 \times 10^4$ rad m^{-2}. The experimental measurement agrees well with the theoretical calculation.

In Fig. 7, we measure α for different TCs. For $l_1 < 0$, α decreases with increasing Δz. If the magnitude of l_1 is big, α varies slowly. If there is no wavefront curvature difference ($\Delta z = 0$), α is vanishingly small. The sign of α changes when Δz varies from the negative to positive, which is

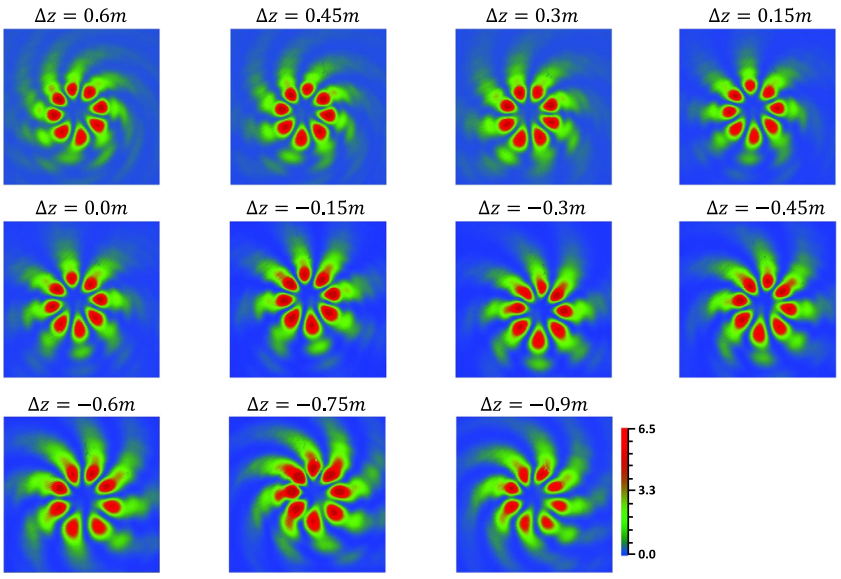

Fig. 5. Twisted interference patterns with different values of Δz. Δz changes from 0.6 m to −0.9 m with a step 0.15 m. $l_1 = -4$.

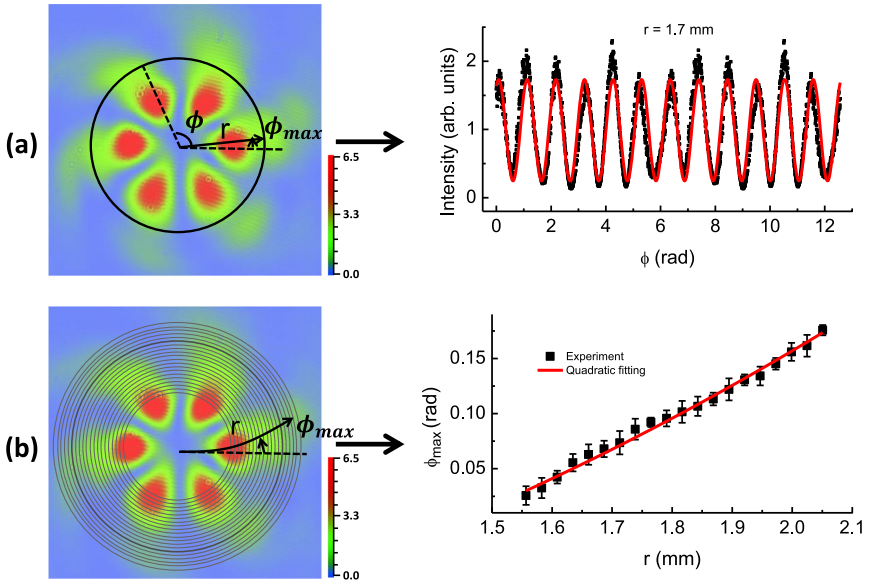

Fig. 6. Measuring the twist coefficient α. $l_1 = -3$, $\Delta z = -0.6$ m. (a) denotes the angular interference fringe with the radius $r = 1.7$ mm. ϕ_{max} is the azimuthal angle for the maximum intensity of the first bright interference fringe. We use a cosine function (red solid curve) to numerically fit the experimental data, extracting $\phi_{max} = 0.086(10)$ rad. (b) plots ϕ_{max} versus r. The red solid curve is the quadratic fitting of Eq. (9), which gives $\alpha = 8.05(17) \times 10^4$ rad m^{-2}. The theoretical value of Eq. (10) is $\alpha = 8.30 \times 10^4$ rad m^{-2}. The black solid circles on the left column schematically indicate the interference paths.

similar to the observations in Fig. 5. The measurements are consistent with the theoretical calculation of Eq. (10).

Several previous works have observed the twist effect of the interference pattern mainly based on the visual inspection [29,37,38]. The work in Ref. [22] has studied the direction of the radial twist from the images of the interference patterns, not providing quantitative information. Here we quantitatively extract the value of ϕ_{max} from the interference fringe and plot the variation of ϕ_{max} along the radial direction. We further measure the twist coefficient α to characterize the degree of the radial twist. Effects of the wavefront curvature difference (denoted with the distance difference Δz) as well as the TC l_1 on the radial twist are systematically explored.

We note that it would be interesting to see the intensity pattern for mixing three or more modes. For three modes, the interference pattern should be more complicated. The interference fringes have three periods determined by $\Delta l_{12} = l_1 - l_2$, $\Delta l_{13} = l_1 - l_3$ and $\Delta l_{23} = l_2 - l_3$. There should exist three twist coefficients (α_{12}, α_{13} and α_{23}) to characterize the degree of the radial twist. Under this condition, the optical ring superlattice will emerge in the intensity distribution, which is the angular counterpart to the general optical superlattice from interfering two pairs of counter-propagating plane-wave laser beams. In optical ring superlattice, by tuning relative phases or intensities of the three modes, people can manipulate atoms in different local sites of the ring [46,47], which has potential applications in quantum simulation and quantum information.

5. Conclusion

In conclusion, compared to the previous works mainly on the visual inspection, we quantitatively characterize the temporal rotation and radial twist of the interference pattern of vortex beams. The effects of the physical parameters (i.e., the TC, frequency difference and

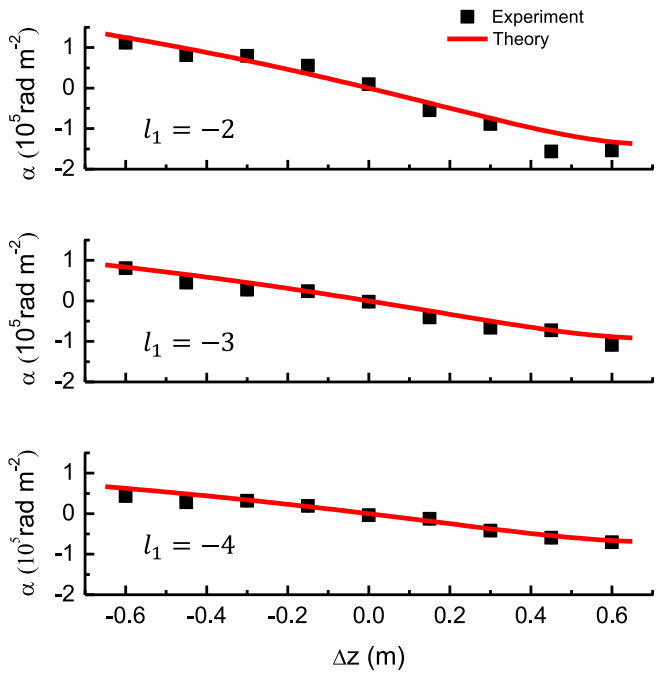

Fig. 7. Twist coefficient α for different TCs. $l_1 = -2, -3, -4$. α is measured as a function of Δz. The error bars are smaller than the data marks. The red solid curves are the theoretical calculations of Eq. (10).

wavefront curvature difference of the vortex beams) on the temporal rotation as well as the radial twist are systematically explored. We measure two parameters, the rotation velocity Ω and twist coefficient α, respectively, to characterize the degree of the temporal rotation and radial twist. The current work is focused on the monochromatic light. Seen from Eqs. (1) and (2), the light phase is dependent on the wavelength. For a spectrally broadband source, like an ultrafast vortex pulse, the interference pattern will be more complicated. Specifically, the wavelength-dependent Gouy phase shift would lead to the so-called spectral Gouy rotation or radial spectral Gouy oscillation [48,49]. On the other hand, the OAM beams generated by the vortex phase plate should be more appropriately described in terms of confluent hypergeometric beams, also called Kummer beams [50], or as combinations of Kummer beams [51]. However, in the far-field zone ($z \gg z_R$) as in our experiment, the intensity distribution is similar to a LG beam, and the expected behavior as a function of frequency and spatial phase differences is expected to be the same as described in the present manuscript. The knowledge of the detailed structure of the interference pattern can extend the application in manipulation of matter using superimposed vortex beams [30,34–36].

Acknowledgments

This work has been supported by the NKRDP (National Key Research and Development Program) under Grant No. 2016YFA0301503, NSFC (Grant No. 11674358, 11904388, 12004398, 12121004), CAS, China under Grant No. YJKYYQ20170025 and K. C. Wong Education Foundation, China (Grant No. GJTD-2019-15), and Hubei province, China under Grant No. 2021CFA027.

Declaration of competing interest

The authors declare that they have no known competing financial interests or personal relationships that could have appeared to influence the work reported in this paper.

References

[1] L. Allen, M.W. Beijersbergen, R.J.C. Spreeuw, J.P. Woerdman, Orbital angular momentum of light and the transformation of laguerre-Gaussian laser modes, Phys. Rev. A 45 (1992) 8185–8189.
[2] M.J. Padgett, L. Allen, The poynting vector in Laguerre-Gaussian laser modes, Opt. Commun. 121 (1-3) (1995) 36–40.
[3] N. Bozinovic, Y. Yue, Y. Ren, P.K.M. Tur, H. Huang, A.E. Willner, S. Ramachandran, Terabit-scale orbital angular momentum mode division multiplexing in fibers, Science 340 (6140) (2013) 1545–1548.
[4] G. Vallone, V.D. Ambrosio, A. Sponselli, S. Slussarenko, L. Marrucci, F. Sciarrino, P. Villoresi, Freespace quantum key distribution by rotation-invariant twisted photons, Phys. Rev. Lett. 113 (6) (2014) 060503.
[5] A.M. Yao, M.J. Padgett, Orbital angular momentum: origins, behavior and applications, Adv. Opt. Photon. 3 (2) (2011) 161–204.
[6] D.G. Grier, A revolution in optical manipulation, Nature 424 (6950) (2003) 810–816.
[7] L. Paterson, M.P. MacDonald, J. Arlt, W. Sibbett, P.E. Bryant, K. Dholakia, Controlled rotation of optically trapped microscopic particles, Science 292 (5518) (2001) 912–914.
[8] A. Lehmuskero, Y. Li, P. Johansson, M. Käll, Plasmonic particles set into fast orbital motion by an optical vortex beam, Opt. Express 22 (4) (2014) 4349–4356.
[9] M. DeMarco, H. Pu, Angular spin–orbit coupling in cold atoms, Phys. Rev. A 91 (3) (2015) 033630.
[10] K. Sun, C. Qu, C. Zhang, Spin–orbital-angular-momentum coupling in Bose–Einstein condensates, Phys. Rev. A 91 (6) (2015) 063627.
[11] H.-R. Chen, K.-Y. Lin, P.-K. Chen, N.-C. Chiu, J.-B. Wang, C.-A. Chen, P.-P. Huang, S.-K. Yip, Y. Kawaguchi, Y.-J. Lin, Spin–orbital-angular-momentum coupled Bose–Einstein condensates, Phys. Rev. Lett. 121 (11) (2018) 113204.
[12] P.-K. Chen, L.-R. Liu, M.-J. Tsai, N.-C. Chiu, Y. Kawaguchi, S.-K. Yip, M.-S. Chang, Y.-J. Lin, Rotating atomic quantum gases with light-induced azimuthal gauge potentials and the observation of the Hess-Fairbank effect, Phys. Rev. Lett. 121 (25) (2018) 250401.
[13] D. Zhang, T. Gao, P. Zou, L. Kong, R. Li, X. Shen, X. Chen, S. Peng, M. Zhan, H. Pu, K. Jiang, Ground-state phase diagram of a spin–orbital-angular-momentum coupled Bose–Einstein condensate, Phys. Rev. Lett. 122 (11) (2019) 110402.
[14] D.P. Ghai, S. Vyas, P. Senthilkumaran, R.S. Sirohi, Detection of phase singularity using a lateral shear interferometer, Opt. Lasers Eng. 46 (6) (2008) 419–423.
[15] D.P. Ghai, S. Vyas, P. Senthilkumaran, R.S. Sirohi, Shearograms of a singular beam using wedge plate lateral shear interferometer, Opt. Lasers Eng. 46 (11) (2008) 797–801.
[16] A.N. Khoroshun, A.V. Chernykh, S.V. Kucher, A.N. Tsymbaluk, Optimal parameters of a shearing interferometer with a singular light source, J. Opt. Technol. 79 (1) (2012) 9–11.
[17] B. Sokolenko, N. Shostka, O. Karakchieva, A. Volyar, D. Poletayev, Determination of microrelief of the sample by singular beams superposition, Comput. Opt. 43 (5) (2019) 741–746.
[18] M.S. Kulya, B. Sokolenko, A. Gorodetsky, N.V. Petrov, Propagation dynamics of ultrabroadband terahertz beams with orbital angular momentum for wireless data transfer, Proc. SPIE 11307 (2020) 113070J.
[19] N.V. Petrov, M. Kulya, A. Gorodetsky, B. Sokolenko, On the features of the interference of a set of broadband uniformly topologically charged beams, Proc. SPIE 11499 (2020) 114990I.
[20] E. Tsiplakova, M. Kulya, A. Gorodetsky, B.V. Sokolenko, N.V. Petrov, Interference enabled binary data encoding within broadband uniformly topologically charged terahertz beams, in: OSA Imaging Appl. Opt. Congr. 2021 (3D, COSI, DH, ISA, PcAOP), OSA, Washington, D.C, 2021, DTh5C.5.
[21] E.G. Tsiplakova, M.S. Kulya, B.V. Sokolenko, A. Gorodetsky, N.V. Petrov, Investigation of spectral encoding with terahertz broadband uniformly topologically charged beams, in: 2021 46th Int. Conf. Infrared, Millim. Terahertz Waves, IEEE, 2021, pp. 1–2.
[22] J. Ma, P. Li, Y. Gu, Characteristics of spiral patterns formed by coaxial interference between two vortex beams with different radii of wavefront curvatures, Photonics 8 (9) (2021) 393.
[23] V.V. Kotlyar, A.A. Kovalev, A.P. Porfirev, Calculation of fractional orbital angular momentum of superpositions of optical vortices by intensity moments, Opt. Express 27 (8) (2019) 11236–11251.
[24] Y. Wang, X. Feng, D. Zhang, P. Zhao, X. Li, K. Cui, F. Liu, Y. Huang, Generating optical superimposed vortex beam with tunable orbital angular momentum using integrated devices, Sci. Rep. 5 (2015) 10958.
[25] I. Moreno, J.A. Davis, T. Womble-Dahl, D.M. Cottrell, Azimuthal multiple-beam interference effects with combinations of vortex beams, Opt. Lett. 40 (10) (2015) 2341–2344.
[26] Z. Bouchal, V. Kollarova, P. Zemanek, T. Cizmar, Orbital angular momentum of mixed vortex beams, Proc. SPIE 6609 (660907) (2007) 660904–660907.
[27] S. Franke-Arnold, J. Leach, M.J. Padgett, V.E. Lembessis, D. Ellinas, A.J. Wright, J.M. Girkin, P. Öhberg, A.S. Arnold, Optical ferris wheel for ultracold atoms, Opt. Express 15 (14) (2007) 8619–8625.
[28] J. Arlt, M. MacDonald, L. Paterson, W. Sibbett, K. Dholakia, K. Volke-Sepulveda, Moving interference patterns created using the angular doppler-effect, Opt. Express 10 (16) (2002) 844–852.

[29] M. Harris, C. Hill, J. Vaughan, Optical helices and spiral interference fringes, Opt. Commun. 106 (4-6) (1994) 161–166.
[30] G. Liang, B. Yuan, Y. Li, X. Kong, W. Cheng, H. Qiao, X. Hu, Evolutions of optical vortices under wide gaussian background, Results Phys. 26 (2021) 104352.
[31] D. Yang, Z. Yang, Z. Zhao, Z. Liu, Radius of curvature of spherical wave measurement based on vortex beam interference, Opt. Lasers Eng. 142 (2021) 106592.
[32] A.H. Dorrah, M. Zamboni-Rached, M. Mojahedi, Experimental demonstration of tunable refractometer based on orbital angular momentum of longitudinally structured light, Light. Sci. Appl. 7 (1) (2018) 40.
[33] Y. Na, D.-K. Ko, High-resolution refractometry using phase shifting interferometry based on spatial light modulator and vortex probe, Opt. Laser Technol. 112 (15) (2019) 479–484.
[34] V.E. Lembessis, A. Alqarni, S. Alshamari, A. Siddig, O.M. Aldossary, Artificial gauge magnetic and electric fields for free two-level atoms interacting with optical Ferris wheel light fields, J. Opt. Soc. Amer. B 34 (6) (2017) 1122–1129.
[35] M. Lacki, H. Pichler, A. Sterdyniak, A. Lyras, V.E. Lembessis, O. Al-Dossary, J.C. Budich, P. Zoller, Quantum hall physics with cold atoms in cylindrical optical lattices, Phys. Rev. A 93 (1) (2016) 013604.
[36] X. He, P. Xu, J. Wang, M. Zhan, Rotating single atoms in a ring lattice generated by a spatial light modulator, Opt. Express 17 (23) (2009) 21007–21014.
[37] S. Cui, B. Xu, S. Luo, H. Xu, Z. Cai, Z. Luo, J. Pu, S. Chávez-Cerda, Determining topological charge based on an improved Fizeau interferometer, Opt. Express 27 (9) (2019) 12774–12779.
[38] J. Vickers, M. Burch, R. Vyas, S. Singh, Phase and interference properties of optical vortex beams, J. Opt. Soc. Amer. A 25 (3) (2008) 823–827.
[39] B. Khajavi, E.J. Galvez, Determining topological charge of an optical beam using a wedged optical flat, Opt. Lett. 42 (8) (2017) 1516–1519.
[40] M.E. Riley, G.M. A, Laser beam divergence utilizing a lateral shearing interferometer, Appl. Opt. 16 (10) (1977) 2753–2756.
[41] R. Geneaux, C. Chappuis, T. Auguste, Radial index of Laguerre-Gaussian modes in high-order-harmonic generation, Phys. Rev. A 95 (5) (2017) 051801.
[42] V.E. Lembessis, E. Vasileios, Atomic ferris wheel beams, Phys. Rev. A 96 (1) (2017) 013622.
[43] S.M. Baumann, D.M. Kalb, L.H. MacMillan, E.J. Galvez, Propagation dynamics of optical vortices due to Gouy phase, Opt. Express 17 (12) (2009) 9818–9827.
[44] N.V. Petrov, P.V. Pavlov, A.N. Malov, Numerical simulation of optical vortex propagation and reflection by the methods of scalar diffraction theory, Quantum Electron. 43 (6) (2013) 582–587.
[45] X. Li, Y. Tai, F. Lv, Z. Nie, Measuring the fractional topological charge of LG beams by using interference intensity analysis, Opt. Commun. 334 (2015) 235–239.
[46] A.M. Rey, K. Burnett, I.I. Satija, C.W. Clark, Entanglement and the mott transition in a rotating bosonic ring lattice, Phys. Rev. A 75 (6) (2007) 063616.
[47] A. Nunnenkamp, A.M. Rey, K. Burnett, Generation of macroscopic superposition states in ring superlattices, Phys. Rev. A 77 (2) (2008) 023622.
[48] M. Liebmann, A. Treffer, M. Bock, T. Elsaesser, R. Grunwald, Spectral anomalies and gouy rotation around the singularity of ultrashort vortex pulses, Opt. Express 25 (21) (2017) 26076–26088.
[49] M. Liebmann, A. Treffer, M. Bock, U. Wallrabe, R. Grunwald, Ultrashort vortex pulses with controlled spectral gouy rotation, Appl. Sci. 10 (12) (2020) 4288.
[50] G. Anzolin, F. Tamburini, A. Bianchini, C. Barbieri, Method to measure off-axis displacements based on the analysis of the intensity distribution of a vortex beam, Phys. Rev. A 79 (3) (2009) 033845.
[51] G. Ruffato, M. Massari, M. Carli, F. Romanato, Spiral phase plates with radial discontinuities for the generation of multiring orbital angular momentum beams: fabrication, characterization, and application, Opt. Eng. 54 (11) (2015) 111307.